Proceedings of the 11th World Congress on Mechanical, Chemical, and Material Engineering (MCM'25)

Paris, France - August, 2025 Paper No. HTFF 231 DOI: 10.11159/htff25.231

Numerical Analysis of a Soft Propeller with Flagellum-Inspired Geometry for Underwater Propulsion

Ilyas Khurshid¹, Mrunal Kanti Mishra^{1,2}, Federico Renda^{1,2}, Francesco Giorgio-Serchi³, Imran Afgan¹

¹Department of Mechanical and Nuclear Engineering, Khalifa University, Abu Dhabi, UAE
²Khalifa University Center for Autonomous Robotic Systems, Khalifa University, Abu Dhabi, UAE
<u>ilyas.khurshid@ku.ac.ae</u>; <u>mrunal.mishra@ku.ac.ae</u>; <u>federico.renda@ku.ac.ae</u>; <u>imran.afgan@ku.ac.ae</u>

³Scottish Microelectronics Centre, The University of Edinburgh, Edinburgh, United Kingdom
f.giorgio-serchi@ed.ac.uk

Abstract - In recent years, soft robots and propellers have emerged as flexible and adaptive alternatives to traditional rigid rotors, offering enhanced morphological versatility and embodied intelligence. However, optimizing their energy efficiency remains a significant challenge. To address this, Reynolds-Averaged Navier–Stokes (RANS) simulations were conducted to investigate fluid-structure interactions around flagellum-inspired geometries. The sliding mesh approach was employed, capturing both transient and mean hydrodynamic loads, such as thrust and torque for two rotating configurations operating at 90 and 60 RPM. This enabled a detailed comparison of their propulsion performance. The 90 RPM propeller, with a diameter of 0.37 m, demonstrated superior performance by generating 0.60 N of thrust, an axial induced velocity of 0.0528 m/s, and a peak flow velocity of 1.72 m/s. However, the 60 RPM configuration, with a slightly larger diameter of 0.40 m, produced a lower thrust of 0.33 N, an induced velocity of 0.0362 m/s, and a peak velocity of 1.26 m/s. Moreover, despite 90 RPM having smaller disk area, achieved a higher local relative velocity of 1.75 m/s and more concentrated flow structures, indicating more efficient energy transfer. These findings highlight the decisive role of rotational speed and geometry in optimizing the performance of soft propellers, with the 90 RPM configuration proving more effective for high-thrust, performance-oriented underwater applications.

Keywords: Design optimization, flagellum, soft propeller, thrust, torque, turbulent flow.

1. Introduction

Soft robotics has emerged as a novel field, offering various systems with embody intelligence through the use of compliant, deformable materials [1-3]. These flexible materials enable soft robots to adapt their shape and behavior in response to external stimuli, making them particularly well-suited for difficult and dynamic environments. In underwater applications, this adaptability of soft robots has inspired the development of soft propulsive modules that mimic locomotion biological species such as bacterial flagella. These flagellum-inspired soft propellers are actuated at the base by a simple rotary motor, allowing the structure to passively deform into a helical shape due to its inherent elasticity. This helical motion of the soft propeller generates thrust as the propeller interacts with the fluid. It is important to mention that the mechanical properties such as density, elasticity and poison's ratio and control parameter could be coupled for enhanced locomotion. Thus, the compliant nature of these robotic systems not only enhances their ability to navigate through harsh and sensitive environments, such as coral reefs or marine ecosystems, but also reduces the risk of damage to both the robot, its moving parts and the surroundings environment [4].

To understand the mechanics and improve the performance of such robotic systems, it is essential to study the complex fluid-structure interactions (FSI) that control and affect their motion [5]. It is important to mention that various empirical methods provide valuable insights. However, the numerical simulations offer a powerful, cost effective and flexible alternative for exploring a wide range of design and control parameters. Various previous studies, such as those by Armanini et al., [3] have demonstrated the effectiveness of model-based design approaches for flagellate propellers. However, due to multiple constraints and assumptions they emphasized the importance of computational tools in evaluating and predicting hydrodynamic performance. Thus, various theoretical approaches such as Blade Element Momentum (BEM) theory, actuator disk and actuator line methods, and hybrid techniques can serve as useful starting points. Nevertheless, to capture the detailed, unsteady flow dynamics and deformation behavior of soft propellers, high-fidelity Computational Fluid Dynamics (CFD) methods are preferred, despite their higher computational cost.

Different techniques are used for modeling, including analytical and numerical approaches [6,7]. In this study, to the best of the authors' knowledge, the Unsteady Reynolds-Averaged Navier–Stokes (URANS) equations were used for the first time in a commercial CFD package (STAR-CCM+) to investigate the hydrodynamic behavior of two flagellum-inspired geometries rotating at different RPMs. By employing the sliding mesh technique, we successfully captured both transient and mean flow characteristics, enabling a detailed assessment of thrust and torque generation. This approach provided critical insights into the design improvement and control optimization of soft underwater propellers, with implications for energy efficiency, maneuverability, and environmental compatibility.

2. Methodology

The following URANS equations are solved through commercial CFD software StarCCM+. The flow is considered transient, incompressible and Newtonian. The mass conservation equation is as follows [7]:

$$\frac{\partial \bar{u}}{\partial x} + \frac{\partial \bar{v}}{\partial y} + \frac{\partial \bar{w}}{\partial z} = 0 \tag{1}$$

Where \bar{u}, \bar{v} and \bar{w} are the mean velocity components in the x, y and z directions, respectively. This equation enforces mass conservation (incompressible flow assumption). The momentum equation is given as:

$$\frac{\partial V_{i}}{\partial t} + V_{i} \frac{\partial V_{i}}{\partial x_{i}} = -\frac{1}{\rho} \frac{\partial P}{\partial x_{i}} + \frac{\partial \bar{w}}{\rho \partial x_{i}} (2\mu \bar{e}_{ij} - \rho V_{i}^{'} V_{j}^{'})$$
(2)

Where V_j is the mean velocity in the ith direction, t is the time, x_j is the spatial time, ρ is the fluid density, P is mean pressure, μ is the dynamic viscosity, \bar{e}_{jj} is the mean rate of strain tensor, V_j' , V_j' are the fluctuating velocity components due to turbulence in directions i and j, respectively, and the term $V_i'V_j'$ presents the Reynolds stress, modeling the turbulent momentum transport. Moreover, in Eq (2), e_{jj} is the tensor strain and is determined from the following relation.

$$\bar{e}_{ij} = \frac{1}{2} \left(\frac{\partial V_i}{\partial x_j} + \frac{\partial V_j}{\partial x_i} \right) \tag{3}$$

According to the Boussinesq assumption, the Reynolds stress can be obtained from the following equation:

$$\tau_{ij} = -\rho V_i^{'} V_j^{'} = 2\mu_t \bar{e}_{ij} - \frac{2}{3}\rho k \delta_{ij}$$

$$\tag{4}$$

Where τ_{ij} is the Reynolds stress tensor (modeled turbulent stresses), μ_t is the eddy viscosity, \bar{e}_{ij} is the mean strain rate tensor, k is the mechanical energy of turbulence, and δ_{ij} is the kronecker delta. We used $k-\varepsilon$ and $k-\omega$ Shear Stress Transport (SST) turbulence model for accurate CFD modeling of the flagellum. As per the findings of the turbulence model study and recommendations of Ali et al. [5], $k-\omega$ SST model was found to be the most suitable eddy-viscosity model for rotor applications.

2.1. Computational domain & boundary conditions

In this study, a sliding mesh technique was employed, where a rotating computational zone surrounding the flagellum was embedded within a stationary cylindrical domain, as illustrated in Fig. 1. The rotating zone had a diameter twice that of the flagellum and was positioned 9D from the inlet, extending 15D upstream from the outlet. The stationary domain measured 25D in length and 15D in diameter, with symmetry boundary conditions applied to its outer surface, along with a stagnation inlet and pressure outlet. A sliding interface between the rotating and stationary zones facilitated data exchange at each timestep, following the method described by Afgan et al. [8]. All flagellum surfaces were treated as no-slip walls with a

resolved surface mesh. Additionally, the grid refinement study is applied to the three grid resolutions. Case A has the coarsest grid, Case B has the medium resolution, and Case C has the finest resolution; see Table 1 for details. In this study, the grid refinement ratio, r for the uniformed meshed is described as:

refinement ratio, r for the uniformed meshed is described as:
$$r = \frac{Total\ No.\ of\ grid\ (Fine)}{Total\ No.\ of\ grid\ (Medium)} = \frac{Total\ No.\ of\ grid\ (Medium)}{Total\ No.\ of\ grid\ (Coarse)} = 2$$
(5)

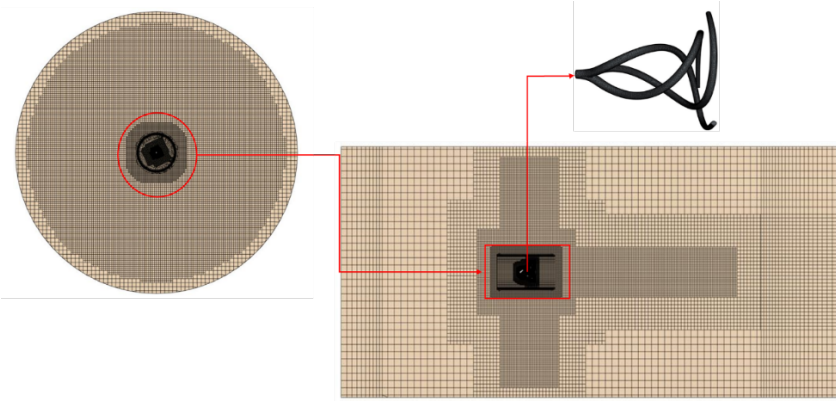


Fig. 1 Computational grid of different zones and a view of the generated boundary mesh of the flagellum

Table 1: Details of mesh and cells total number for mesh sensitivity study

| S.No | Mesh | Base/local leng | Total number of cells | | |
|------|--------|-----------------|-----------------------|-------------|---------|
| | type | Flagella | Rotating zone | Static zone | |
| 1 | Coarse | 0.0125 | 0.025 | 0.025 | 302444 |
| 2 | Medium | 0.00625 | 0.0125 | 0.025 | 1094761 |
| 3 | Fine | 0.00312 | 0.00625 | 0.025 | 1667220 |

The refinement ratio is higher than the minimum value of 1.3 and the order of accuracy is determined by applying the following equation.

$$p = \frac{\ln \frac{\varepsilon_{32}}{\varepsilon_{21}}}{\ln(r)} \tag{6}$$

Where ε the error tolerance is determined by the following equation

$$\varepsilon_{i+1,i} = f_{i+1} - f_i \tag{7}$$

Moreover, the convergence conditions of this system must be clarified first to assess the extrapolated value from the equations above. The convergence conditions are Monotonic convergence, and they prevail when 0 < R < 1, Oscillatory convergence when R < 1 and Divergence when R > 1. where R is the convergence ratio, given as $R = \varepsilon_{21}/\varepsilon_{32}$. It is important to mention that for monotonic convergence, the generalized Richardson Extrapolation equation is applied to estimate the errors and uncertainties, presented in Equation (7).

Table 2: The Grid Convergence Index (GCI) and various parameters of accuracy for thrust, drag and torque

| Parameters | E ₃₂ | \varepsilon_{21} | R | Behaviour | p | GCI ₂₁ (| <i>GCI</i> ₃₂ (|
|------------|------------------------|-------------------------|-------|-----------------------|------|---------------------|----------------------------|
| | | | | | | %) | %) |
| Thrust | 0.139 | 0.022 | 0.158 | Monotonic Convergence | 5.33 | 0.45 | 2.78 |

| Drag | 0.132 | 0.018 | 0.138 | Monotonic Convergence | 5.72 | 0.24 | 1.71 |
|--------|-------|-------|-------|-----------------------|------|------|------|
| Torque | 0.110 | 0.020 | 0.182 | Monotonic Convergence | 4.92 | 0.52 | 2.80 |

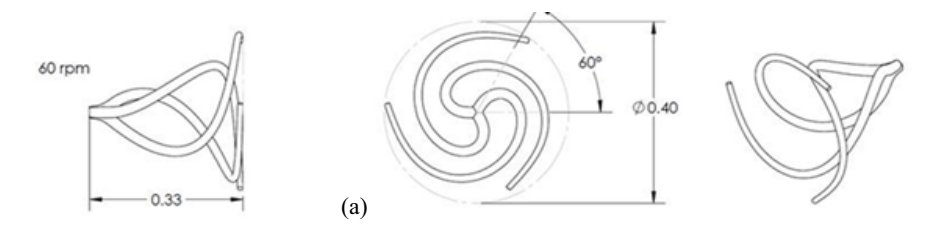
For oscillatory convergence, the results display some oscillations and for divergence, the results diverge while errors and uncertainties are impossible to be determined. Table 2 shows the results for order of accuracy for thrust, drag and torque. The results are calculated from three different types of mesh. It is evident from the results presented in Table 2 that the convergence conditions for thrust, drag, and torque are monotonic as the value of convergence ratio, R is more than zero and less than 1 for all cases. Hence these parameters are applicable in the Grid Convergence Index (GCI) method. This method is a valuable contribution to the systematic and most common methodology to determine grid refinement or independence. Moreover, the GCI is based on the grid refinement error estimator derived from the generalized Richardson Extrapolation. The percentage of differences between the computed and asymptotic values is calculated by using GCI. It demonstrates how the value of the error is computed with the asymptotic value and how much the solution of the computed value would change with further refinement. Thus, a small value of GCI percentage shows the computed value is approaching asymptotic range. The GCI for fine grid can be interpreted by the following equation.

$$GCI_{i+1,i} = F_{SI_{\overline{f_i}(I^p-1)}}^{|\mathcal{E}_{i+1,i}|} \tag{8}$$

where F_S is the safety factor and for the three different grids used in this study, the safety factor is kept at 1. The results presented in Table 2 shows that the various GCI parameters for thrust, drag, and torque for the various meshes are in good agreement with the decrement value from GCI_{32} to GCI_{21} , where $(GCI_{21} < GCI_{32})$. The results demonstrate that the dependency of numerical method on the mesh size has been decreased because the GCI value for the finer grid (GCI_{21}) is lower than the coarser grid (GCI_{32}) . Therefore, the results of simulation are grid independent as further refinement of the grid will not lead to considerable change. Hence, the fine mesh was used for all remaining simulations and validation with the experimental data.

3. Results and discussions

The following two geometries of the flagellum are selected for analysis; both are made up of same material but rotating at different RPMs 60 and 90 as shown in Fig. 2. The stiffness of the filament material is characterized by a Young's modulus, E of 1 MPa, Poison's ratio as 0.5, and density of 1120 kg/m³, and material damping = 10000 Pa.s which was found to yield favorable thrust generation and shape adaptation [9]. It is evident from Fig. 2, that the 60 RPM configuration features a larger diameter of 0.40 meters and a width of 0.33 meters, suggesting a broader interaction with the surrounding fluid. However, the 90 RPM propeller is more compact, with a diameter of 0.37 meters and a width of 0.30 meters, which likely contributes to more focused thrust generation and improved rotational efficiency. These geometric differences play a key role in influencing the hydrodynamic performance and energy transfer characteristics of each design.



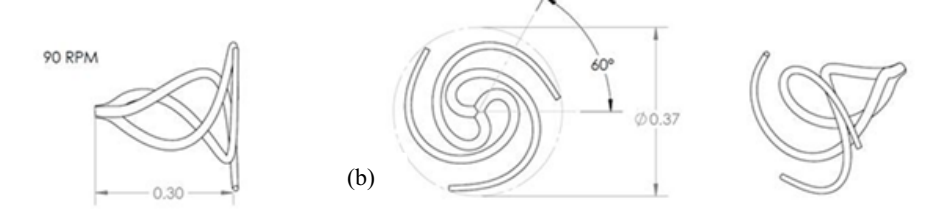


Fig. 2 Comparison of geometries used for CFD analysis (a) Geometry-60RPM, (b) Geometry-90 RPM

Fig. 3 (a) illustrates the transient thrust performance for the two geometries. This time-history plot of thrust reveals that both flagellum geometries exhibit fluctuating thrust generation over time, typical of soft robotic systems with flexible structures. At 90 RPM, the blue curve shows consistently higher thrust magnitude compared to the 60 RPM case. The 90 RPM geometry generates transient thrust values frequently exceeding 0.5 N and occasionally peaking near 1.0 N, while the 60 RPM geometry remains mostly below 0.5 N with less pronounced peaks. These fluctuations suggest stronger fluid-structure interactions and increased unsteady forces at higher rotational speeds, contributing to enhanced propulsive force.

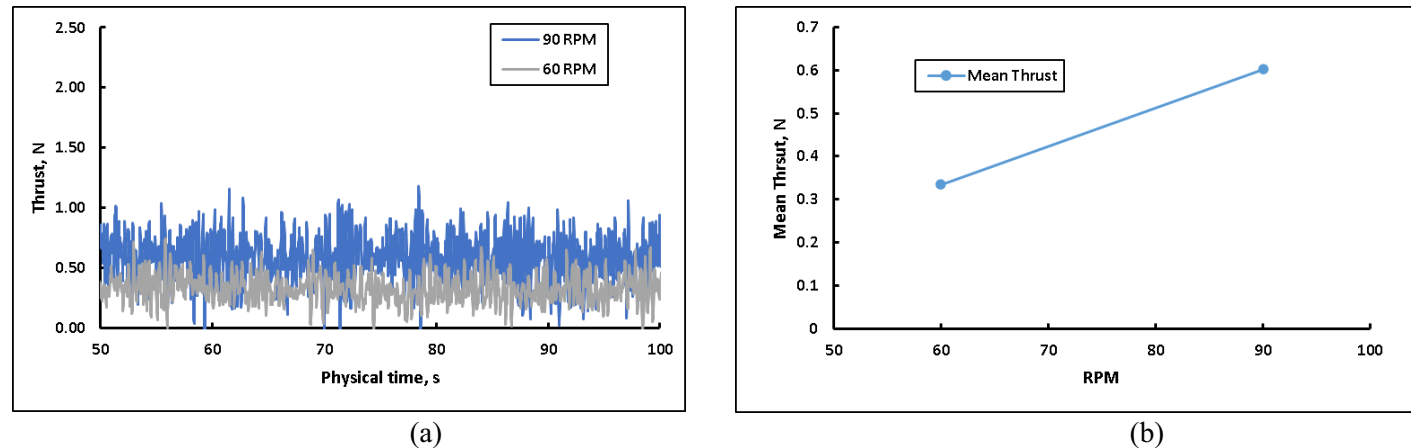


Fig. 3 Thrust performance of two geometries (a) Instantaneous thrust profile (b) mean thrust

The mean thrust comparison of the two geometries is presented in Fig. 3(b). The mean thrust analysis clearly indicates that the geometry operating at 90 RPM outperforms the 60 RPM configuration. As seen in the mean thrust plot, the higher speed geometry produces an average thrust of approximately 0.6 N, compared to just 0.35 N at 60 RPM. This 70% increase in mean thrust highlights the impact of rotational speed and geometry optimization on propulsion efficiency. However, while higher thrust is beneficial, the corresponding energy input and potential reduction in efficiency must be considered during design trade-offs, especially for applications requiring sustained operation or battery-powered actuation.

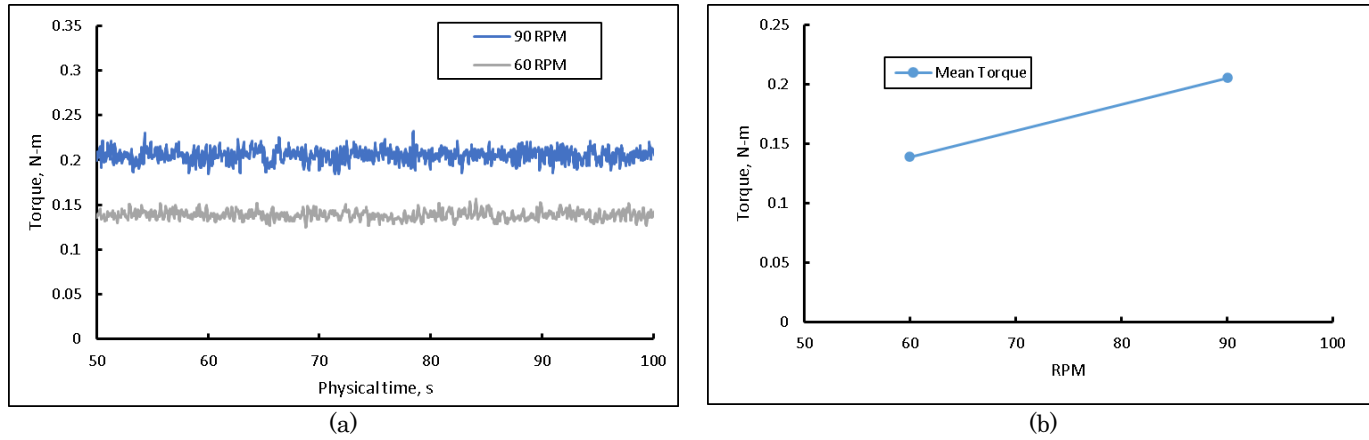


Fig. 4 Torque performance of two geometries (a) Instantaneous torque profile (b) mean torque

The transient torque plot for the two geometries presented in Fig.4(a) illustrates a clear difference in torque demand between the two geometries at different rotational speeds. The flagellum operating at 90 RPM consistently generates higher torque values, with fluctuations centered around 0.22–0.25 N·m. In contrast, the 60 RPM configuration exhibits more stable and lower torque values, averaging around 0.15 N·m. This trend indicates that while increasing the rotational speed enhances thrust, it also demands more torque input, which can affect the motor selection and power consumption. The relatively steady nature of both curves implies stable mechanical performance, but the higher torque required at 90 RPM must be balanced against overall system efficiency, especially for energy-constrained or portable robotic platforms.

The mean torque comparison of the two geometries is presented in Fig. 4(b). This Figure illustrates the variation in mean torque as a function of rotational speed (RPM). The data reveals a clear increase in torque output with higher rotational speed, where the configuration operating at 90 RPM achieves a mean torque of approximately $0.205~\rm N\cdot m$, compared to $0.139~\rm N\cdot m$ at $60~\rm RPM$. This 47% increase in torque suggests enhanced mechanical performance at elevated speeds, which may contribute to improved propulsion characteristics. These findings underscore the importance of optimizing rotational speed in the design of torque-driven systems, particularly in applications where mechanical efficiency and output are critical.

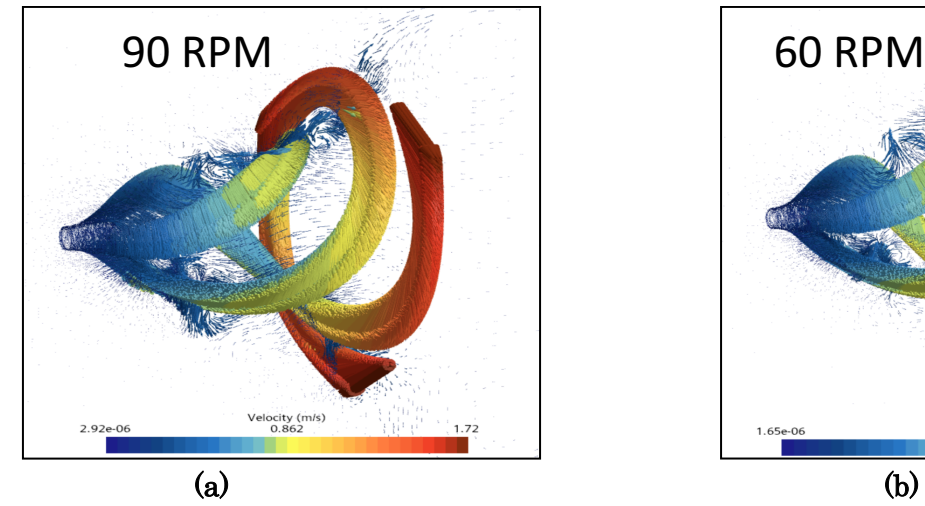


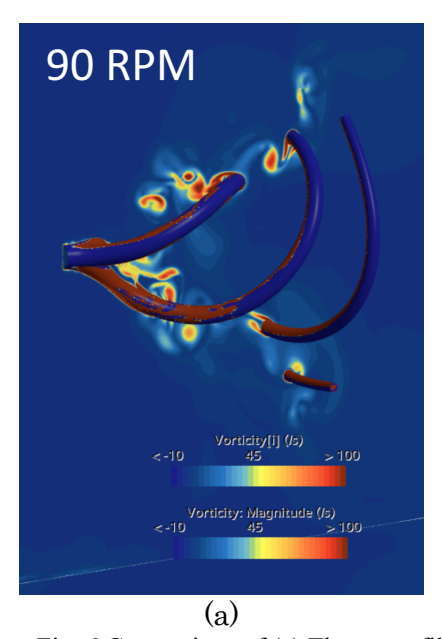
Fig. 5 Velocity Field Comparison with Streamline Visualization at (a) 90 RPM and (b) 60 RPM

Velocity (m/s) 0.628

Figure 5 presents the velocity field distributions for two rotational speeds: (a) 90 RPM and (b) 60 RPM. The color contours represent velocity magnitudes in meters per second (m/s), with streamlines overlaid to indicate flow direction and

structure. At 90 RPM, the velocity field exhibits a broader range, with peak velocities reaching approximately 1.72 m/s, compared to a maximum of 1.26 m/s at 60 RPM. This increase in peak velocity at higher RPM is accompanied by more pronounced and complex flow structures, as evidenced by the denser and more curved streamlines in Fig. 5 (a). In contrast, the 60 RPM configuration shows a more subdued flow field with lower overall velocity magnitudes and less dynamic streamline behavior. These observations suggest that increasing rotational speed enhances fluid acceleration and induces stronger flow circulation, which may contribute to improved propulsion or mixing performance depending on the application. The results underscore the importance of rotational speed in influencing flow dynamics and system efficiency.

Figure 6 displays the vorticity field distributions at two rotational speeds: (a) 90 RPM and (b) 60 RPM. The color contours represent vorticity magnitude in s⁻¹, with a scale ranging from below -10 to above 100. At 90 RPM, the vorticity field exhibits significantly higher intensity and more localized regions of strong rotational motion, as indicated by the broader presence of red and orange zones. This suggests, enhanced shear and rotational effects in the fluid, likely due to the increased angular momentum imparted by the higher rotational speed. In contrast, the 60 RPM configuration shows a more diffused vorticity distribution with lower peak values, indicating weaker rotational dynamics. These results highlight the influence of rotational speed on the generation and distribution of vorticity, which is critical for understanding mixing, propulsion, and flow stability in rotating systems.



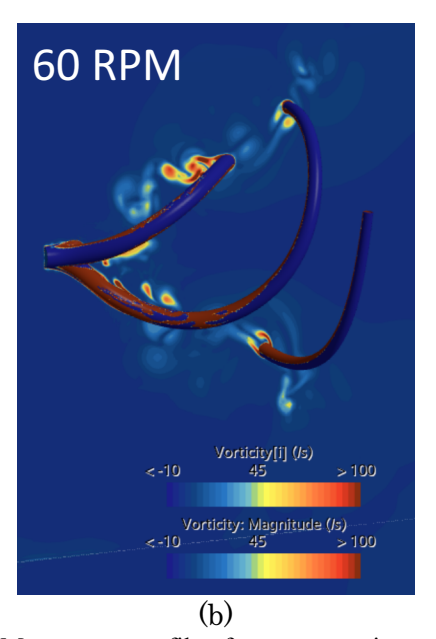


Fig. 6 Comparison of (a) Thrust profile of two geometries, (b) Momentum profile of two geometries

Thus, based on a comprehensive analysis of hydrodynamic parameters presented in Table 3. It is evident from flow characteristics, and theoretical modeling that the 90 RPM configuration demonstrates superior overall efficiency and performance compared to the 60 RPM setup. Despite having a slightly smaller diameter (0.37 m vs. 0.40 m), the 90 RPM propeller achieves a higher average thrust (0.33 N vs. 0.60 N), which directly translates into a greater axial induced velocity of approximately 0.0528 m/s, as calculated using momentum theory. This is a result of both the higher rotational speed and the smaller disk area (0.1075 m² vs. 0.1257 m²), which concentrates the flow and increases the energy imparted to the fluid. Additionally, the angular velocity at 90 RPM is significantly higher (9.42 rad/s compared to 6.28 rad/s), which enhances the tangential velocity component and contributes to a higher local relative velocity at the blade tip (1.75 m/s vs. 1.26 m/s).

Table 3. Comparison of Hydrodynamic Parameters at 90 RPM and 60 RPM

| | Parameter | Equation | 90 RPM | 60 RPM |
|--|-----------|----------|--------|--------|
|--|-----------|----------|--------|--------|

| Radius, m | R = D/2 | 0.185 | 0.20 |
|------------------------------|---|--------|--------|
| Disk Area, m ² | $A = \pi r^2$ | 0.1075 | 0.1257 |
| Axial Induced Velocity, m/s | $V_i = \sqrt{\frac{T_{ij}}{2\rho A}}$ | 0.0528 | 0.0362 |
| Angular Velocity, rad/s | $\Omega = \frac{2\pi . RPM}{60}$ | 9.42 | 6.28 |
| Local relative velocity, m/s | $U_{rel} = \sqrt{(2 v_i)^2 + (\Omega R)^2}$ | 1.75 | 1.26 |
| Peak flow velocity, m/s | From CFD streamline | 1.72 | 1.26 |
| | visualization | | |

These theoretical findings are corroborated by CFD streamline visualizations, which show that the 90 RPM configuration produces a peak flow velocity of 1.72 m/s, substantially greater than the 1.26 m/s observed at 60 RPM. This indicates a more energetic and focused wake, which is beneficial for propulsion efficiency. While the 60 RPM configuration benefits from a larger disk area that may reduce induced losses and be advantageous in low-speed, high-load scenarios, its lower thrust output and reduced flow acceleration limit its effectiveness in dynamic or high-performance applications. Therefore, the 90 RPM configuration is clearly more efficient in converting rotational energy into thrust and is better suited for applications requiring compact design, high thrust, and effective energy transfer, making it the preferred choice for performance-critical underwater propulsion systems.

4. Conclusions

This study presents, for the first time, a comparative hydrodynamic analysis of two soft propeller configurations operating at 90 RPM and 60 RPM, using momentum theory, local velocity analysis, and CFD-based flow visualization. The results show that the 90 RPM configuration, despite having a slightly smaller diameter, outperforms the 60 RPM setup in terms of thrust generation, axial induced velocity, and peak flow velocity. Specifically, the 90 RPM propeller achieved a higher average thrust of 0.60 N, an axial induced velocity of 0.0528 m/s, and a peak flow velocity of 1.72 m/s. In contrast, the 60 RPM configuration, with a larger diameter, produced a lower thrust of 0.33 N, an induced velocity of 0.0362 m/s, and a peak velocity of 1.26 m/s. Additionally, the local relative velocity at the blade tip was higher for the 90 RPM setup (1.75 m/s) compared to 1.26 m/s for the 60 RPM case, indicating more effective energy transfer. These improvements are attributed to the higher angular velocity and more concentrated flow dynamics in the 90 RPM design. While the 60 RPM configuration may be better suited for low-speed, energy-efficient applications due to its larger disk area, the 90 RPM setup offers superior performance and efficiency for high-thrust, compact propulsion systems. Overall, the analysis highlights the importance of optimizing rotational speed and geometry to enhance underwater propeller efficiency, with the 90 RPM configuration emerging as the more effective choice for performance-driven applications.

Acknowledgements

This research was supported by Khalifa University of Science and Technology, Under Research & Innovation Grant, Award No. [RIG-2023-048], and Research Center Grant [RCII-2019-003]. The authors would also like to thank Khalifa University of Science and Technology for providing the HPC resources.

References

- [1] C. Laschi, B. Mazzolai, and M. Cianchetti, "Soft robotics: Technologies and systems pushing the boundaries of robot abilities," *Science Robotics*, vol. 1, no. 1, Art. no. eaah3690, 2016.
- [2] G. Alici, "Softer is harder: What differentiates soft robotics from hard robotics?," *MRS Advances*, vol. 3, no. 28, pp. 1557–1568, 2018.

- [3] C. Armanini, M. Farman, M. Calisti, F. Giorgio-Serchi, C. Stefanini, and F. Renda, "Flagellate underwater robotics at macroscale: Design, modeling, and characterization," *IEEE Transactions on Robotics*, vol. 38, no. 2, pp. 731–747, 2022.
- [4] K. C. Galloway, K. P. Becker, B. Phillips, J. Kirby, S. Licht, D. Tchernov, R. J. Wood, and D. F. Gruber, "Soft Robotic Grippers for Biological Sampling on Deep Reefs," Soft Robotics, vol. 3, no. 1, pp. 23–33, 2016.
- [5] Q. S. Ali and M.-H. Kim, "Unsteady aerodynamic performance analysis of an airborne wind turbine under load varying conditions at high altitude," *Energy Conversion and Management*, vol. 210, Art. no. 112696, 2020, doi: 10.1016/j.enconman.2020.112696.
- [6] I. Khurshid and J. Choe, "An analytical model for dissolution of deposited asphaltene during CO₂ injection from the porous media," *International Journal of Oil, Gas and Coal Technology*, vol. 19, no. 3, pp. 338–352, 2018. https://doi.org/10.1504/IJOGCT.2018.093143.
- [7]. H. K. Versteeg and W. Malalasekera, *An Introduction to Computational Fluid Dynamics: The Finite Volume Method*, Harlow, UK: Pearson Education, 2007.
- [8] I. Afgan, J. McNaughton, S. Rolfo, D. D. Apsley, T. Stallard, and P. Stansby, "Turbulent flow and loading on a tidal stream turbine by LES and RANS," *International Journal of Heat and Fluid Flow*, vol. 43, pp. 96–108, 2013.
- [9] A. S. AlShehhi, C. Armanini, A. T. Mathew, D. Feliu-Talegon, and F. Renda, "Trident: A Multi-Functional Soft Appendage for Underwater Locomotion and Grasping," *IEEE Robotics and Automation Letters*, vol. 10, no. 1, pp. 436–443, 2025, doi: 10.1109/LRA.2024.3504238.